Laboratory-based multi-modal X-ray microscopy and micro-CT with Bragg magnifiers

P. Vagovič,[1,*] **D. Korytár,**[2] **A. Cecilia,**[3] **E. Hamann,**[3] **T. Baumbach,**[3] **and D. Pelliccia**[4,5,6]

[1]*Center for Free-Electron Laser Science, Deutsches Elektronen-SYnchrotron, Hamburg, Germany*
[2] *Institute for Electrical Engineering, Slovak Academy of Sciences, Bratislava, Slovakia*
[3] *ANKA Light Source, Karlsruhe Institute of Technology, Karlsruhe, Germany*
[4] *School of Applied Sciences, RMIT University, Victoria 3001, Australia*
[5] *Australian Synchrotron, Victoria 3168, Australia*
[6] *School of Physics and Astronomy, Monash University, Victoria 3800, Australia*
[*]patrik.vagovic@desy.de

Abstract: We report on the successful demonstration of X-ray phase contrast microscopy and micro computed tomography (CT) with a Bragg magnifier microscope (BMM) in a laboratory setup. The Bragg magnifiers, constituted by two channel-cut crystals in asymmetric diffraction, produced a 15X magnification of the X-ray beam, thus enabling high resolution imaging to be attained. The angular sensitivity of the crystals was used to implement analyzer-based phase contrast imaging: acquiring images at different angular positions and the three parametric images (apparent absorption, differential phase and scattering) have been obtained. Micro-CT, with resolution of about 5 μm is demonstrated with the same system. The main limitations, as well as the ways to mitigate them, are discussed with the aid of the experimental data. The technique demonstrated herein extends high-resolution, multi-modal, x-ray imaging and micro-CT to compact laboratory setups, with the potential of broadening the reach of these techniques outside the community of synchrotron users.

OCIS codes: (340.7440) X-ray imaging; (340.0340) X-ray optics; (110.0180) Microscopy; (110.6955) Tomographic imaging.

References and links

1. W. J. Boettinger, H. E. Burdette, and M. Kuriyama, "X-ray magnifier," Rev. Sci. Instrum. **50**, 26–30 (1979).
2. E. Dobročka, "Geometrical principles of the monolithic x-ray magnifier," J. Appl. Crystallogr. **24**, 212–221 (1991).
3. Y. Kagoshima, Y. Tsusaka, K. Yokoyama, K. Takai, S. Takeda, and J. Matsui, "Phase-contrast x-ray imaging using both vertically and horizontally expanded synchrotron radiation x-rays with asymmetric bragg reflection," Japan. J. Appl. Phys. **38**, L470 (1999).
4. K. Kobayashi, K. Izumi, H. Kimura, S. Kimura, T. Ibuki, Y. Yokoyama, Y. Tsusaka, Y. Kagoshima, and J. Matsui, "X-ray phase-contrast imaging with submicron resolution by using extremely asymmetric Bragg diffractions," Appl. Phys. Lett. **78**, 132–134 (2001).
5. P. Schäfer and R. Köhler, "Asymmetric Bragg reflection as X-ray magnifier," J. Phys. D: Appl. Phys. **36**, A113–A117 (2003).
6. D. Korytár, P. Mikulík, C. Ferrari, J. Hrdý, T. Baumbach, A. Freund, and A. Kuběna, "Two-dimensional x-ray magnification based on a monolithic beam conditioner," J. Phys. D: Appl. Phys. **36**, A65 (2003).

7. A. Andreev, V. Asadchikov, A. Buzmakov, A. Konovko, S. Kuzin, A. Pertsov, Y. Ponomarev, R. Senin, I. Smirnov, S. Shestov, and V. Shkurko, "Two-dimensional image magnification in an asymmetric-reflection x-ray microscope," JETP Lett. **85**, 98–100 (2007).

8. P. Vagovič, D. Korytár, P. Mikulík, A. Cecilia, C. Ferrari, Y. Yang, D. Hänschke, E. Hamann, D. Pelliccia, T. A. Lafford, M. Fiederle, and T. Baumbach, "In-line bragg magnifier based on v-shaped germanium crystals," J. Synchrotron Radiat. **18**, 753–760 (2011).

9. M. Stampanoni, G. Borchert, and R. Abela, "Progress in microtomography with the bragg magnifier at {SLS}," Radiat. Phys. Chem. **75**, 1956 – 1961 (2006).

10. K. Hirano, "Application of x-ray image magnifier and demagnifier to parallel beam x-ray computed tomography," J. Phys. D: Appl. Phys. **44**, 055501 (2011).

11. P. Vagovič, D. Korytár, A. Cecilia, E. Hamann, L. Švéda, D. Pelliccia, J. Härtwig, Z. Zápražný, P. Oberta, I. Dolbnya, K. Shawney, U. Fleschig, M. Fiederle, and T. Baumbach, "High-resolution high-efficiency x-ray imaging system based on the in-line bragg magnifier and the medipix detector," J. Synchrotron Radiat. **20**, 153–159 (2013).

12. K. Hirano, Y. Takahashi, and H. Sugiyama, "Development and application of variable-magnification x-ray bragg magnifiers," Nucl. Instrum. Meth. A **741**, 78–83 (2014).

13. P. Vagovič, L. Švéda, A. Cecilia, E. Hamann, D. Pelliccia, E. Gimenez, D. Korytár, K. Pavlov, Z. Zápražný, M. Zuber, T. Koenig, M. Olbinado, W. Yashiro, A. Momose, M. Fiederle, and T. Baumbach, "X-ray bragg magnifier microscope as a linear shift invariant imaging system: image formation and phase retrieval," Opt. Express **22**, 21508–21520 (2014).

14. M. Servidori, F. Cembali, and S. Milita, "3d dumond diagrams of multi-crystal bragg-case synchrotron topography. I. Flat sample," Appl. Phys. A Mater. Sci. Process. **73**, 75–82 (2001).

15. T. Davis, D. Gao, T. Gureyev, A. Stevenson, and S. Wilkins, "Phase-contrast imaging of weakly absorbing materials using hard x-rays," Nature **373**, 595–598 (1995).

16. D. Chapman, W. Thomlinson, R. Johnston, D. Washburn, E. Pisano, N. Gmür, Z. Zhong, R. Menk, F. Arfelli, and D. Sayers, "Diffraction enhanced x-ray imaging," Phys. Med. Biol. **42**, 2015 (1997).

17. M. N. Wernick, O. Wirjadi, D. Chapman, Z. Zhong, N. P. Galatsanos, Y. Yang, J. G. Brankov, O. Oltulu, M. A. Anastasio, and C. Muehleman, "Multiple-image radiography," Phys. Med. Biol. **48**, 3875 (2003).

18. L. Rigon, F. Arfelli, and R.-H. Menk, "Three-image diffraction enhanced imaging algorithm to extract absorption, refraction, and ultrasmall-angle scattering," Appl. Phys. Lett. **90**, 114102 (2007).

19. P. Modregger, D. Lübbert, P. Schäfer, and R. Köhler, "Two dimensional diffraction enhanced imaging algorithm," Appl. Phys. Lett. **90**, 193501 (2007).

20. M. Hönnicke and C. Cusatis, "Analyzer-based x-ray phase-contrast microscopy combining channel-cut and asymmetrically cut crystals," Rev. Sci. Instrum. **78**, 113708 (2007).

21. K. Hirano, Y. Takahashi, and H. Sugiyama, "Application of variable-magnification x-ray bragg magnifier to analyzer-based phase-contrast computed tomography," Jpn. J. Appl. Phys. **53**, 040302 (2014).

22. D. Vine, D. Paganin, K. Pavlov, J. Kraeusslich, O. Wehrhan, I. Uschmann, and E. Foerster, "Analyzer-based phase contrast imaging and phase retrieval using a rotating anode x-ray source," Appl. Phys. Lett. **91**, 254110 (2007).

23. W. Zhou, K. Majidi, and J. G. Brankov, "Analyzer-based phase-contrast imaging system using a micro focus x-ray source," Rev. Sci. Instrum. **85**, 085114 (2014).

24. A. Authier, *Dynamical Theory of X-ray Diffraction* (Oxford University, 2004).

25. D. Korytár, P. Vagovič, C. Ferrari, and P. Šiffalovič, "X-ray Crystal Optics based on Germanium Single Crystals," in *Germanium: Characteristics, Sources and Applications.*, (Nova Science Publishers, 2013), pp. 105-140.

26. D. M. Paganin, "Coherent X-Ray Optics", (Oxford University Press, New York, 2006).

27. D. Sayre and H. N. Chapman, "X-ray microscopy," Acta Crystallogr. Sect. A **51**, 237 (1995).

28. A. Momose, "Phase–sensitive imaging and phase tomography using X-ray interferometers," Opt. Express **11** 2303 (2003).

29. F. Pfeiffer, C. Kottler, O. Bunk and C. David, "Hard X-ray phase tomography with low-brilliance sources," Phys. Rev. Lett. **98**, 108105 (2007).

30. L. Rigon, H.-J. Besch, F. Arfelli, R.-H. Menk, G. Heitner, and H. Plothow-Besch, "A new dei algorithm capable of investigating sub-pixel structures," J. Phys. D: Appl. Phys. **36**, A107 (2003).

31. M. M. Hall, Jnr, V. G. Veeraraghavan, H. Rubin, and P. G. Winchell, "The approximation of symmetric X-ray peaks by Pearson type VII distributions," J. Appl. Crystallogr. **10**, 66–68 (1977).

32. M. J. Kitchen, K. M. Pavlov, K. K. W. Siu, R. H. Menk, G. Tromba, and R. A. Lewis, "Analyser-based phase contrast image reconstruction using geometrical optics," Phys. Med. Biol. **52**, 4171 (2007).

33. A. Buades, B. Coll, and J.-M. Morel, "Non-local means denoising," IPOL **1**, 217–246 (2011).

1. Introduction

The recent development of X-ray instrumentation and techniques, in combination with highly efficient X-ray optics and detectors, is enabling laboratory imaging and microscopy experiments, which were so far possible only at the synchrotron sources, on compact setups. Amongst numerous proposed optical schemes, X-ray magnification based on asymmetric Bragg diffraction has long been studied [1,2] for its ability to expand or compress an x-ray beam and thus to tailor its phase-space properties. The use of two-dimensional Bragg magnifiers, firstly reported in late 1970s [1], were studied with synchrotron and laboratory X-ray sources [1–7]. More recently, thanks to advances in detection technology and crystal quality, x-ray imaging and microscopy based on x-ray Bragg magnifiers (reffered in text as Bragg Magnifier Microscope, BMM) became a reliable alternative to conventional approaches [8]. Recent results demonstrated the impressive capabilities of an BMM [9–13] for high resolution x-ray microscopy, holography and micro-CT (computed tomography), with synchrotron sources. In this work we report on the experimental demonstration of X-ray microscopy with Bragg Magnifier in a conventional X-ray laboratory setup.

A BMM is based on the asymmetric diffraction from a crystal, providing 1D X-ray beam magnification. Further, 2D magnification is achieved by combining two crystals (or two sequences of crystals) in a crossed configuration (so-called σ-π configuration know from X-ray topography [14]).

Notably, the magnification is not the only feature of the BMM that makes it extremely interesting for x-ray imaging. The use of a crystal in (asymmetric) Bragg diffraction conditions, naturally reminds of analyzer-based x-ray imaging (ABI) techniques. The reflectivity profile of a crystal about its Bragg position ('rocking curve') constitute a common way to measure angular beam deviations produced by a sample placed in front of the crystal [15]. This property has been used for the quantitative estimation of attenuation, phase and scattering contrast produced by a sample illuminated by an x-ray beam [16–18]. Importantly the ABI approach has been successfully used with Bragg magnifiers [19–21].

ABI techniques with symmetric crystal diffraction have recently been applied to compact, laboratory x-ray sources [22,23]. This step paves to way to make ABI techniques available to a larger scientific community, enabling multiple contrast sensitivity for applications in medical imaging and the life sciences that traditionally falls outside the synchrotron users community.

The main reason for the inefficiency of BMMs in laboratories is the fact that laboratory sources generate divergent polychromatic beams: A BMM on the other hand requires a highly collimated and monochromatic beam. The angular acceptance of a BMM (see for instance [24]) is typically between ~20 – ~400 μrad depending on the photon energy, magnification factor (asymmetry), crystal material and the reflection used. Further, the spectral acceptance $\delta E/E$ is of the order of 10^{-4} for a BMM because it is essentially a crystal monochromator. Therefore, as for most of high resolution X-ray microscopy techniques, the efficiency of an BMM critically depends on the *brilliance* of the x-ray source. Hence the most convincing demonstration of the techniques employing BMM needed the third generation synchrotron sources.

We here show how to maximize the efficiency of BMM, by coupling a brilliant rotating anode X-ray source with collimating X-ray optics [25] and an efficient detector. In this way we can efficiently employ a BMM in a laboratory setup for phase contrast and tomography applications.

2. Experimental setup

The measurements were carried out at the X-ray Microscopy and Nano-Diffraction laboratory at Monash University. The characteristic Cu K_α radiation from the source (Rigaku FR-E + Super Bright) was preliminarily collimated by a two-dimensional parabolic multilayer mirror (AXO-

Dresden) resulting in a X-ray beam with divergence about 1 mrad. Subsequently the X-ray beam was pre-monochromated (and further collimated) by a channel-cut (symmetric) crystal monochromator Ge(111) to select the Cu K_{α_1} line (x-ray wavelength $\lambda = 0.154$ nm). Due to the angular acceptance of the monochromator and the incoming beam divergence, K_{α_2} contamination was still present after the monochromator amounting to about 15% of Cu K_{α_1} (data not shown). The small contamination was subsequently filtered by the last Ge(220) magnifier, diffracting in the vertical plane. The filtering was achieved due the σ-π crystal configuration of the Ge(111) monochromator and the Ge(220) channel-cut crystal magnifying in the vertical direction. The use of a monochromatic beam is mandatory to employ ABI reconstruction techniques. A slit placed in the front of the monochromator was used to set the beam size to 1mm X 1mm, approximately equal to the spatial acceptance of the BMM. A guard slit, placed in front of the sample downstream the monochromator was used to cut residual scattering from the upstream optics. The sample was located immediately after the guard slit and mounted on a tomographic stage. Two asymmetric V-shaped Ge 220 channel-cut crystals were placed after the sample. The measured value of the magnification was 15X. Data have been collected with an Andor I-Kon CCD working in direct conversion mode, i.e. without the use of a scintillating screen, with a pixel size of 13.5 μm. We used 2x2 binning, thus the effective pixel size after the X-ray magnification was 1.8 μm. The schematic of the setup is depicted in Fig 1.
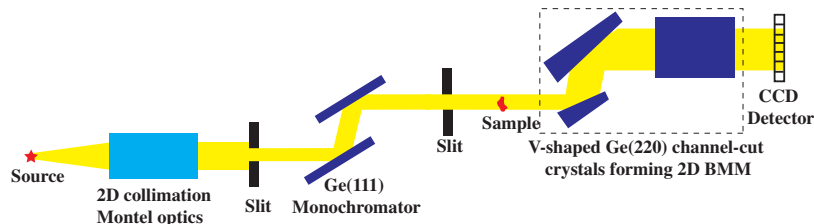

Fig. 1. Schematics sketch of the experimental setup (top view). Two channel-cut crystals are placed just after the sample, first one is magnifying in horizontal direction and the second in vertical direction. The magnification was 15-fold.

With the horizontally and the vertically diffracting crystals being placed consecutively – i.e. their distance from the sample being different – the effective propagation distance is different in the horizontal and vertical direction. This is directly affecting the resolution, which turns out to be different in the two directions. To understand this point we must briefly review the principles of image formation in a Bragg Magnifier Microscope. More details can be found in [13].

Each crystal is producing a magnified version of the wave field that is incident upon its surface. The incident wave field is different from the wave front right after the sample: the propagation in free space from the sample to the crystal surface modulates the wave field introducing a phase factor that is quadratic with the transverse coordinates (see for instance [26]). The effect of the modulation is the appearance of interference fringes (Fresnel fringes) around the sample edges. In the near-edge and Fresnel diffraction regime, the period of the fringes can be much smaller (1-100 nm scale or below) than the resolution of the imaging system, while the fringes can significantly extend across the sample features. Therefore, though not directly detected, the fringes produce an effective blurring of the acquired image.

The blurring due to diffraction effects is a sort of 'coherent blurring' and is generally concurrent to the 'incoherent blurring' caused by the penumbral effects of the finite source size

(or, as in our case, finite divergence). The two effects could be in principle distinguished by an ideal detector which would measure the blurring of the Fresnel fringes due to penumbral effects, i.e. the partial coherence. In practice, the additional blurring introduced in the detection does not permit, at the resolution level attainable in our experiment, to distinguish between the two contributions. At any rate, both blurring effects increase with the propagation distance [27] and therefore the image produced by the downstream magnifier (vertical direction in our case) has poorer resolution compared to the image with the closer magnifier.

To exemplify this effect in our experimental setup we report, in Fig. 2(a), the image of a gold TEM mesh (G600TT, SPI Supplies) with 600 lines/inch, period of 42 μm, thin bars width of 10 μm and thick bars width of 16 μm.
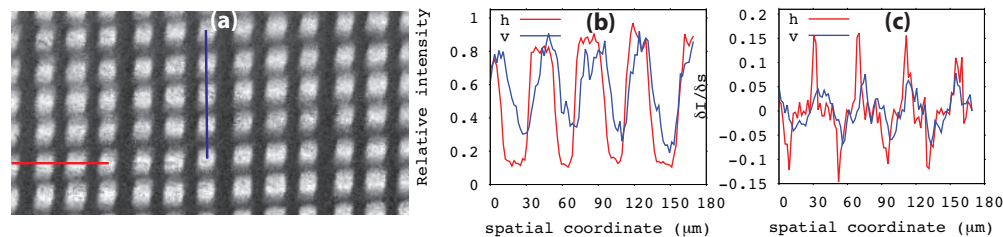
Fig. 2. The image of the TEM mesh (G600TT, SPI Supplies) (a) and the line profiles extracted from the image indicated by the lines in (a). The contrast of the grid pattern measured in horizontal direction is ~74% while in vertical direction ~45%. The derivatives of the profiles (c) suggest the spatial resolution in horizontal direction of ~4μm and in the vertical direction ~5μm.

The apparent blurring of the grid lines in the vertical direction, shown on the profile curves [in Fig. 2(b)], is evident. The contrast of grid pattern in vertical direction is reduced to about 45% while in horizontal direction it is 75%. As expected, the blurring is more evident in the vertical direction due to the larger propagation distance between the sample and the second magnifier. The derivatives of the horizontal and vertical profiles shown in Fig. 2(b) suggest that the spatial resolution in horizontal direction is about 4μm and in vertical it is about 5μm.

3. Tri-modal contrast microscopy and 3D imaging

The inherent astigmatism of the system described above can be minimized by reducing the distance between the two crystals, but obviously cannot be altogether removed. Thus it must be accounted for when designing a system for ABI and micro-CT, and indeed it dictates the choice of the system geometry.

The primary constraint is the resolution (blurring) argument described above. The image at the first magnifier is less affected by blurring and by Fresnel fringes because the first crystal is closer to the sample. In other words the magnified image produced at the first crystal is a more faithful version of the sample image. Therefore it is advisable to use the close crystal as analyzer.

Subsequently the diffraction plane for the analyzer crystal is chosen to be orthogonal to the rotation axis for tomography. This is a common choice in x-ray differential phase contrast tomography [28] where one is interested to obtain phase sensitivity in the reconstructed slices which are orthogonal to the rotation axis. In addition to that, it has been shown that as simple variation of the filtered back-projection approach enables obtaining phase tomography from differential phase projection. This is done by using the so called Hilbert filter [29] in place of

the usual ramp (or similar) filter in the filtered back-projection algorithm. In our experimental situation we were constrained to have the tomography axis in the vertical direction, hence the first crystal was aligned to diffract in the horizontal plane.

Another important aspect to keep in mind when designing an ABI system composed of asymmetric analyzers is that towards the higher magnifications the slope of the input rocking curves becomes less steep when compared to the rocking curve of a symmetric crystal. As a consequence the angular sensitivity is reduced as compared to symmetric analyzer. Therefore the selection of the analyzer magnification is not entirely free and it depends on the required angular resolution. The radiation passing through the sample is deflected in general into two directions due to refraction. If the analyzer crystal is placed downstream the sample then the measured intensity at the detector is modulated by the rocking curve of the analyzer and the angular deviation of the refracted beam is translated into the detected intensity modulation.
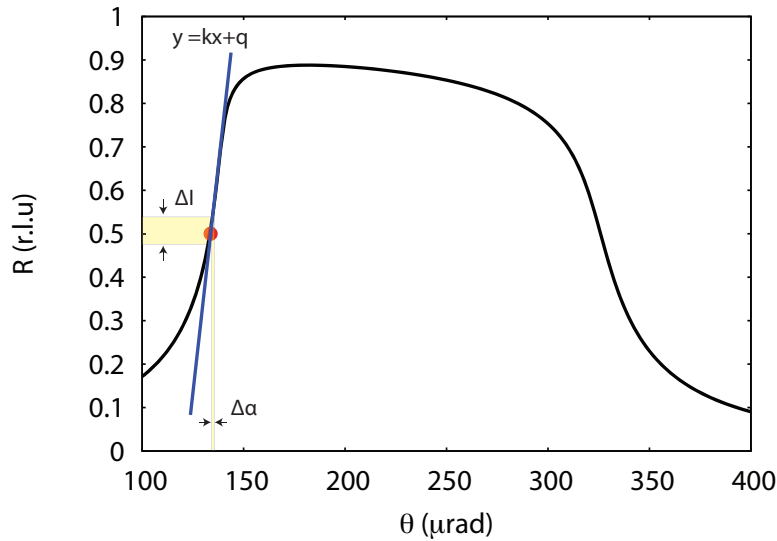

Fig. 3. Modulation of the detected intensity diference at the flank of the rocking curve by the refraction angle difference.

To estimate minimum detectable phase difference we can assume that sample is causing small phase gradients, therefore we can approximate the modulation function of the analyzer by linear approximation at given angular position [Fig. 3]. Under this assumption the relation between minimal detectable refraction angle difference $\Delta\alpha$ is given by

$$\Delta\alpha = -\frac{\lambda}{2\pi}\frac{d\phi(x)}{dx}, \tag{1}$$

where ϕ if the phase. Using the equation above combining with detectable contrast at the detector we can write relation between the phase derivative and the rocking curve slope

$$\frac{d\phi(x)}{dx} = -\frac{2\pi}{\lambda}\frac{\Delta I}{k}, \tag{2}$$

where k is the slope of the rocking curve and ΔI is the detectable intensity difference. Clearly with increasing asymmetry the minimum detectable phase difference is increasing due to decreasing of the rocking curve slope. Using relation above we estimated the minimum detectable

phase difference for the Ge(220) reflection as a function of the asymmetry angle at 8047.78 eV (CuK$_{\alpha 1}$) for several contrasts at the left flank of the rocking curves. The result is shown in the figure 4. The phase sensitivity of the analyzer with asymmetry angle of 19° used in this experiment was estimated to be dϕ/dx $\approx$ 48.92 mrad/μm at photon energy of 8047.78 eV for the contrast of 5%.
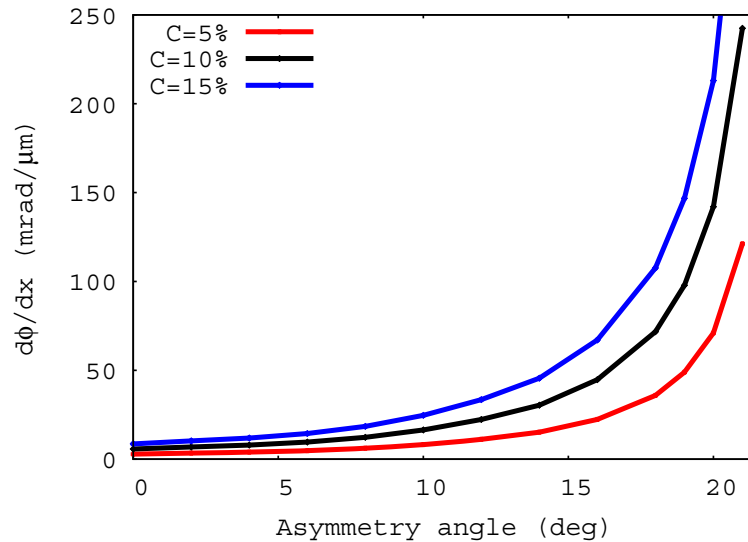

Fig. 4. Phase difference as a function of the asymmetry angle for Ge(220) reflection at photon energy 8047.78 eV, where C is the detectable contrast.

To obtain tri-modal contrast information (apparent absorption, refraction and scattering) with the ABI technique, we collected several images along the rocking curve of the crystal, both with the sample and without it. The sample is constituted by the tip of a dandelion seed (*Taraxacum officinale*). The normalization procedure however proved to be more complicated than the usual flat–field correction because of the presence of two sources of artifacts. The first was represented by the imperfections on the crystal surface which resulted in regions of slightly different intensity across the image, whose behaviour was angle-dependent. The second was an alignment problem, having the rocking axis not exactly lying on the crystal surface. The combinations of those effects produced a small apparent shift of the sample position with respect to the background during the rocking scan. Without proper corrections, such a shift would produce artifacts in the post-processed images using the DEI algorithm, and therefore we devised a procedure to account and correct for this problem.

Every sample raw image has been first normalized by the empty beam image and, in a second instance, normalized by the intensity of the global rocking curve at the corresponding angular position. The global rocking curve was measured from the radiograms without the sample. The normalized images of the tip of the dandelion seed at selected angular positions, along with the global rocking curve, are shown in Fig. 5. As expected, the image acquired around the peak position is dominated by attenuation, while refraction is visible for the flank images. On the other hand a strong scattering component appears in the images taken at the tail of the rocking curve.

Despite the obvious differences, all the images shown always contain a mixture of attenuation, refraction and scattering contrast. To separate the three contribution we used the three–
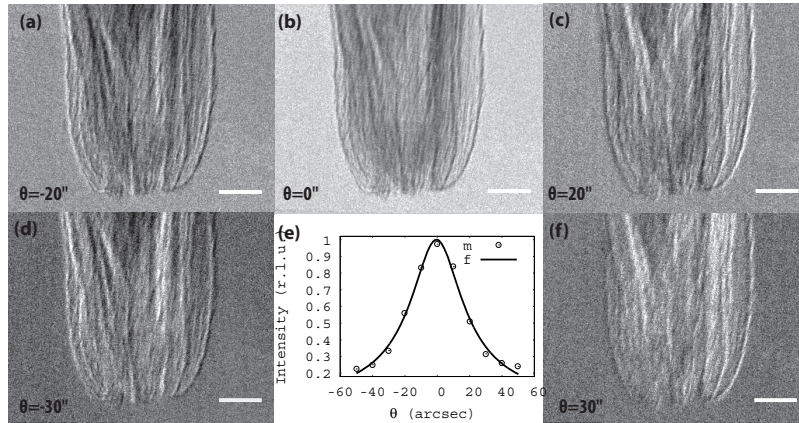
Fig. 5. Images taken at different angular positions of the rocking curves (a,b,c,d,f). Corresponding angle θ is shown in each image. The scale bars correspond to 100μm. Global rocking curve taken from full detector area without the sample (open circles) and the numerical fit with Pearson function of type VII (solid line) are shown in figure (e).

image algorithm (generalized diffraction enhanced algorithm, GDEI) introduced by Rigon *et al.* [30]. For that we fitted the normalized global rocking curve with Pearson VII type function, which provides an excellent approximation of experimental rocking curves [31] and has been successfully applied in the past in conjunction with DEI algorithm [32]. The functional form of the curve is $y = c[1 + (x - \mu)^2/(ma^2)]^{-m}$ and the parameters found in the fit were $c = 1.0$, $a = 0.0001$, $\mu = 0.0$ and $m = 0.7195$.

Using this procedure we extracted three parametric images: (i) apparent absorption image, (ii) refraction angle image (differential phase image) and (iii) ultra-small angle scattering image [Fig. 6]. The apparent absorption image [Fig. 6(a)] clearly contains propagation-based phase contrast as well. The edge-enhancement (see also the corresponding line profile in the inset) shows at least one Fresnel oscillation across the edge of the sample. The profile through the edge on refraction angle image [in Fig. 6(b)] is showing typical differential phase signal however the differential phase contrast is relatively reduced by the strong scattering of the sample as seen from the ultra–small angle scattering map [Fig. 6(c)]. It is worth noting that the sample orientation was chosen in order to have the scattering fibres of the dandelion seed aligned in the vertical direction.
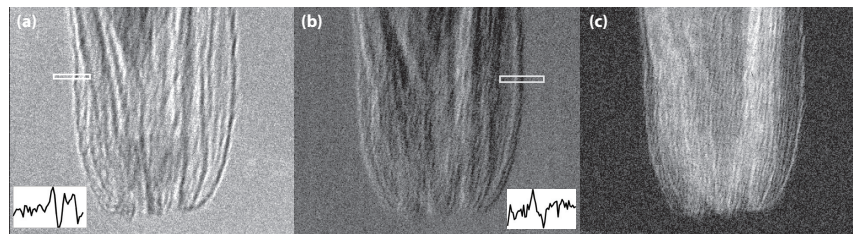

Fig. 6. Apparent absorption image (a), refraction angle image (b) and the scattering image (c) extracted from three images recorded at the peak position ($\theta = 0$), at $\theta = -30$ arcsec and at $\theta = +30$ arcsec using GDEI algorithm. The marked areas at (a) and (b) were used to plot the profile indicated as inlets in corresponding images.

Aligning the first crystal at the peak of the rocking curve, we run a tomography scan of the same sample. Due to the effective parallel beam geometry – the divergence of the magnified beam is reduced by the same magnification factor with respect to the input beam divergence –, only 180°sample rotation is necessary to obtain full 3D information. We recorded 500 projections and the acquisition time was 120s for each projection leading to total scan time of 17h. A single projection is shown in Fig. 7(a).
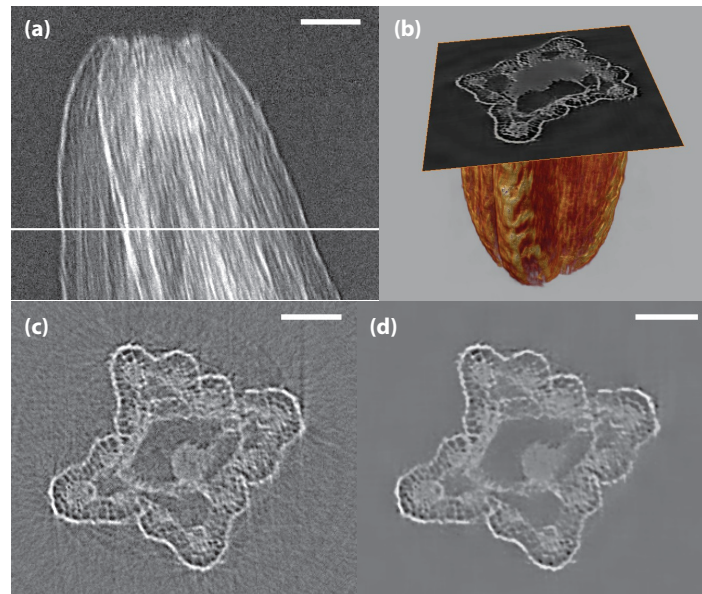

Fig. 7. Figure (a) is showing the negative logarithm projection image normalized by the empty beam image and the 3D rendering is shown on figure (b) . Figures (c) and (d) are the reconstructed axial slices before and after NLM filtering at the position indicated by the line on figure (a). CT reconstruction was done using FBP algorithm. Scale bars correspond to 100 μm. The rendering was done using NLM filtered axial slices.

For the CT reconstruction we used standard filtered back projection algorithm and the reconstructed slices were further processed by non local means de-noising (NLM) [33]. Figure 7(c) shows an example of reconstructed slice, taken at the vertical position marked by the white line in the panel (a). The corresponding slice after de-noising is shown in Fig. 7(d). The rendering was done using AMIRA software using filtered axial slices. The rendering result is shown in Fig. 7(b).

4. Conclusion

In conclusions, we successfully demonstrated high resolution phase-sensitive X-ray microscopy and tomographic imaging with Bragg magnifiers on a compact setup. The results were possible due to the combination of a high brilliant laboratory X-ray source with a carefully designed optical system featuring 2D collimating Montel mirrors, germanium channel-cut monochromators and asymmetrically cut germanium channel-cut crystals acting as Bragg magnifiers for the x-ray beam. We would like to point out that by using this technique the sample is irradiated by highly monochromatic beam, which is very interesting especially for the X-ray imaging of weak, radiation damage sensitive samples. By the optimization described in this work, we achieved that all the photons outside spectral acceptance of BMM, which are not passing

through the BMM (and thus not contributing to the contrast) are filtered out prior to the sample. The technique demonstrated herein extends and broadens the applicability of the Bragg magnifier microscopy to laboratory sources. Thus it has the potential to be used by broader scientific communities outside those of synchrotron users.

Acknowledgments